# Membrane Rejection of Nonspherical Particles: Modeling and Experiment

**Basavaraju Agasanapura and Ruth E. Baltus**
Dept. of Chemical and Biomolecular Engineering, Clarkson University, Potsdam, NY 13699

**Charan Tanneru**
Dept. of Civil and Environmental Engineering, University of Houston, Houston, TX 77204

**Shankararaman Chellam**
Depts. of Civil and Environmental Engineering and Chemical and Biomolecular Engineering,
University of Houston, Houston, TX 77204

*DOI 10.1002/aic.14114*

*The rejection coefficient of nonspherical particles from ultrafiltration and microfiltration membranes has been examined from both theoretical and experimental perspectives. Modeling efforts focused on incorporating the convective hindrance factor for a capsule shaped particle in a cylindrical pore into predictions of the rejection coefficient. First, the convective hindrance factor was approximated using previously reported results for the hydrodynamic resistances experienced by a sphere in a pore. Second, computational fluid dynamics calculations predicted the convective hindrance factor for a capsule in a cylindrical pore. Results from both approaches indicate that including hydrodynamic interactions in predictions of the rejection coefficient has a greater effect for smaller particles and particles with smaller aspect ratio (i.e., close to spherical shape). Rejections of several rod-shaped Gram negative bacteria with aspect ratio from 2 to 5 by clean track-etched membranes were in general agreement with theoretical predictions.* © 2013 American Institute of Chemical Engineers *AIChE J*, 59: 3863–3873, 2013
*Keywords: membrane separations, transport, bioseparations, water treatment, virus and bacteria removal*

## Introduction

Microfiltration and ultrafiltration processes are extensively employed in various fields such as clinical applications, dairy processing, biotechnological applications, water and wastewater treatment, and microelectronic applications.[1] Of particular relevance to environmental engineering applications is the prevention of waterborne disease such as the 1993 *Cryptosporidium* outbreak in Milwaukee, WI that caused over 400,000 illnesses, 1000 hospitalizations, and 50 deaths.[2] Several literature reports indicate that microfiltration or ultrafiltration systems achieve complete separation of protozoa but not bacteria and viruses.[3–7] Although microbial retention can be increased by employing membranes with smaller pore sizes, such an approach also concomitantly increases capital and energy costs by necessitating larger membrane area and higher pressures. Developing a quantitative understanding of the factors determining bacteria and virus removal is the first step toward optimizing the membrane pore size necessary to economically produce biologically stable water.[8]

Efforts to theoretically analyze retention of particles by a porous membrane date back several decades, with studies focused primarily on spheres.[9–12] Because pathogenic bacteria and viruses present in feed waters are often nonspherical, a comprehensive model of membrane separations for such biological colloids is needed to design efficient membrane systems that balance microbial removal with energy and economic considerations.

A general expression for the filtration rejection coefficient $\sigma_f$ includes both hydrodynamic particle-pore wall interactions and steric restrictions with a Boltzmann distribution to describe particle concentration[11]

$$\sigma_f = 1 - \frac{\int\int G(X,\psi)v(X)e^{\left(\frac{-E(X,\psi)}{kT}\right)}dXd\psi}{\int v(X)dX} \tag{1}$$

Here, $G(X, \psi)$ is the local lag coefficient, which represents the hydrodynamic particle-pore wall interactions, $v(X)$ is the fluid velocity field when the particles are excluded from the pore region, $E(X, \psi)$ is the particle-pore wall interaction energy, $X(x, y)$ is the two-dimensional (2-D) position vector in the pore, and $\psi$ is the particle orientation angle with respect to the pore axis.

Early analyses of hindered transport were focused on uncharged spheres using a centerline approximation ($G(X) = G(0)$).[9,13] Brenner and Gaydos[14] developed an

---

Additional Supporting Information may be found in the online version of this article

Correspondence concerning this article should be addressed to R. E. Baltus at baltus@clarkson.edu.

analytical expression for *G(X)* which is valid for relatively small spheres. Ennis et al.[15] used a Padé approximation to combine the small particle expression developed by Brenner and Gaydos[14] with a large particle expression developed by Bungay and Brenner.[13] Numerical simulations were carried out by Higdon and Muldowney[16] who also fit their results to provide an analytical expression for *G(X)*. Dechadilok and Deen[17] used this expression to determine radially averaged hindrance factors as a function of relative particle size which were in excellent agreement with the expression developed by Ennis et al.[15]

Anderson[11] theoretically examined the transport of capsule shaped particles in a cylindrical pore by considering only configurational effects (i.e., $G(X,\psi)=1$ was assumed for all particle positions and orientations). The rejection coefficient for a capsule-shaped particle was predicted to be larger (higher removals) than for a spherical particle with equivalent volume, with rejection coefficient increasing as particle aspect ratio increases.

In a recent article,[8] we described results from short-term membrane rejection measurements that were performed to examine the removal of two gram-negative bacteria (*Brevundimonas diminuta* and *Serratia marcescens*), two bacteriophages (PRD1 and T4), and several spherical silica particles. These (bio) colloids ranged from spherical to capsule shaped, with aspect ratio in the range 1–9. Track etch membranes with well-defined capillary pores with a tight pore-size distribution were used for these measurements. In contrast to Anderson's predictions,[11] similar reflection coefficient values were measured for particles of the same dimensionless size but with different aspect ratios. We speculated that this might be attributed to hydrodynamic particle-pore wall interactions which were neglected in the model.

The objective of this work was to perform detailed theoretical analyses of the convective transport of a rigid capsule shaped particle in a cylindrical pore, yielding predictions of $\sigma_f$ for these particles. Specifically, we have determined $G(X,\psi)$ using two different approaches. As a first approximation, the results of Higdon and Muldowny[16] describing $G(X)$ for spherical particles were incorporated into the Anderson model[11] that considers the steric limitations for a capsule in a pore. Because only one size parameter characterizes the sphere geometry, we considered different size parameters when using the sphere model to quantify the hydrodynamic interactions for a capsule: the diameter of a sphere with volume equivalent to the capsule volume, the diameter of a sphere equal to the capsule length and the diameter of a sphere equal to the capsule diameter. To develop a more comprehensive model of this system, computational fluid dynamic (CFD) calculations based on a finite element model were used to determine $G(0,\psi)$ for a capsule shaped particle in a cylindrical pore. These values were used in equation 1, along with steric restrictions for a capsule to predict $\sigma_f$ for particles with different size and aspect ratio.

Modeling results were validated by short-term measurements of the removal of three rod-shaped bacteria (*Brevundimonas diminuta, Serratia marcescens,* and *Escherichia coli*), two spherical bacterial viruses (MS2 and PRD1) as well as four different spherical silica particles by a number of track-etched membranes with near cylindrical pore geometry in a stirred cell before the onset of fouling.

## Theoretical Work

### *Rejection coefficient*

The filtration rejection coefficient, $\sigma_f$ is a measure of the degree of solute rejection by a porous membrane. The geometry of the system considered here is illustrated in Figure 1. The pore is cylindrical, with length $L$ and radius $R$. The length and diameter of the capsule shaped particle are $L_p$ and $d_p$, respectively. The solvent is treated as a continuum and the flow is dictated by an axial pressure gradient. In this work, Eq. 1 was simplified for a capsule shaped particle-cylindrical pore system, following the procedure described by Anderson[11]

$$\sigma_f=1-\frac{8}{\pi}\int_0^{\frac{\pi}{2}}\int_0^{\alpha_{\max}}\int_0^{\beta_{\max}}G(\alpha,\beta,\psi)\left[\alpha^2+\beta^2+1\right]d\beta d\alpha\sin(\psi)d\psi$$

$$\alpha=\frac{x}{R}\quad\beta=\frac{y}{R}\quad\alpha_{\max}=\sqrt{R^{*2}-L^{*2}}\quad\beta_{\max}=\sqrt{R^{*2}-\alpha^2}-L^{*2}$$

$$L^*=(\varepsilon-1)\lambda\sin(\psi)\quad R^*=1-\lambda\quad\varepsilon=\frac{L_p}{d_p}\quad\bar{X}=\bar{X}(\alpha,\beta)\quad\lambda=\frac{d_p}{2R}\tag{2}$$

Here, $\psi$ is the orientation angle between the particle and the pore axis, and $\bar{X}$ are the nondimensional position vectors. The integration limits $\alpha_{\max}$ and $\beta_{\max}$ are based on the sterically allowed orientations and positions for a capsule in a cylindrical pore. Details of the derivation of Eq. 2 from Eq. 1 are provided in Appendix A.

As an initial approximation for $G(\alpha,\beta,\psi)$, expressions developed by Higdon and Muldowney[16] for spherical particles (i.e., for $G(\alpha,\beta)$) in a cylindrical domain were incorporated into Eq. 2. Integrations over $\alpha$, $\beta$, and $\psi$ were performed to predict $\sigma_f$. Calculations were performed using different characteristic particle sizes to describe $G(\alpha,\beta)$.

Accurately predicting the lag coefficient for a capsule shaped particle in a channel is a complex nonlinear problem which cannot be solved analytically. In this article, we establish a 3-D CFD model which simulates the translation of a capsule-shaped particle in a cylindrical channel. The model is used to solve for the steady-state particle velocity ($v_p$) at a fixed radial position ($\bar{X}$) and orientation ($\psi$). The lag coefficient is defined as the ratio of the steady-state particle velocity to the fluid velocity in the absence of the particle ($u_s$)[17,18]

$$G(\bar{X},\psi)=\frac{\mathbf{v_p}}{\mathbf{u_s}}\tag{3}$$

In this analysis, the computation of $G(\bar{X},\psi)$ is limited to a single, rigid, capsule shaped particle translating on the pore axis ($\bar{X}=0$) at all sterically allowed orientations for relative particle radii ranging from 0 to 0.9. The fluid behavior in the cylindrical channel is described using the Navier-Stokes equation. The motion of the particle is governed by the fluid forces surrounding the particle.

This is a typical fluid-particle interaction problem, where the coupled movement of fluid and particle are analyzed. Previous reports in the literature demonstrate that the Arbitrary Lagrangian Eulerian (ALE) approach is effective for simulating such fluid-particle interaction problems.[19,20] The current CFD analysis includes a 3-D finite element model that predicts the translational velocity of a capsule-shaped particle at a fixed orientation suspended in a fluid in a

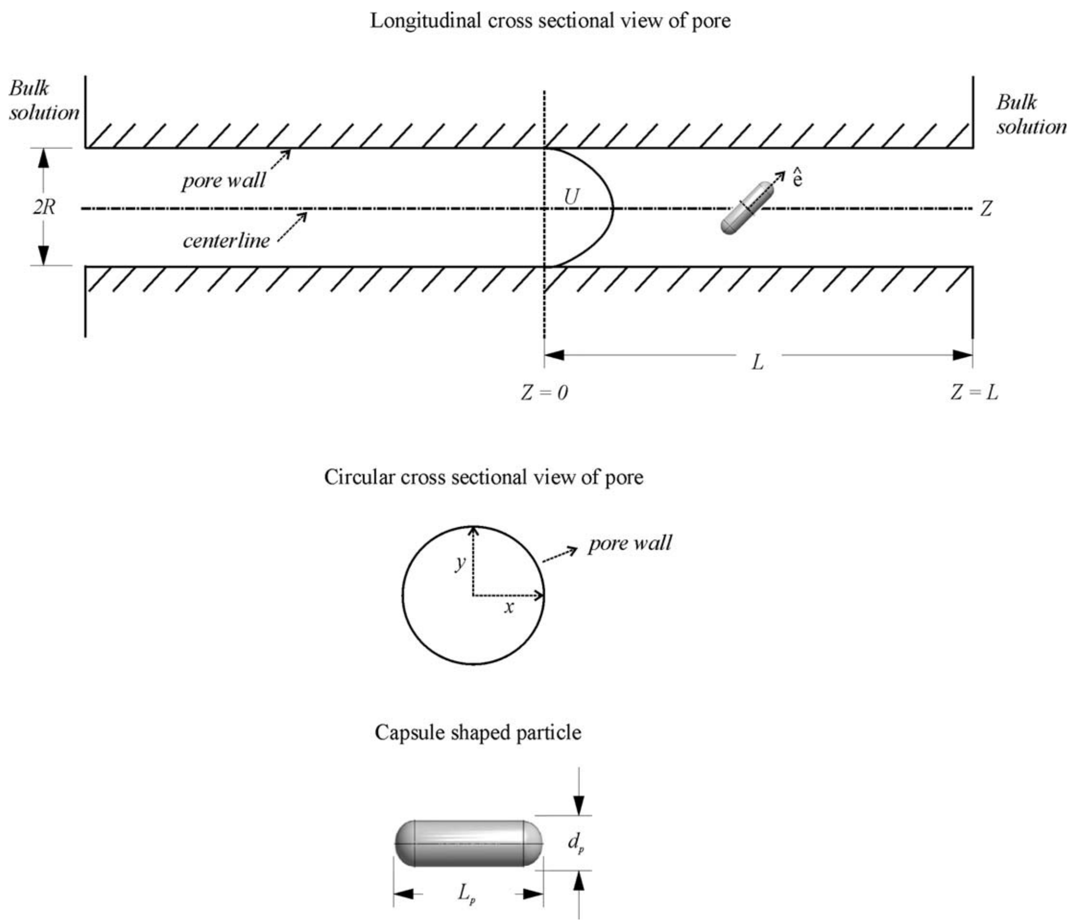
Longitudinal cross sectional view of pore

Circular cross sectional view of pore

Capsule shaped particle

**Figure 1. Schematic diagram of rigid capsule-shaped particle in a cylindrical pore.**

cylindrical channel. The coupling of the Navier- Stokes equation in ALE formulation with Newton's momentum equation enables one to track the particle motion. Since this method involves a moving mesh, the Laplace equation was solved simultaneously with the Navier-Stokes equation to ensure mesh smoothing. The model equations were solved for the normal and shear forces, which were integrated over the particle surface to obtain the resultant hydrodynamic forces.[18–22] These forces are used in Newton's momentum equation to calculate the particle velocity. The lag coefficient $G(0,\psi)$ was then computed from Eq. 3.

A number of assumptions were made in our model development. A steady parabolic flow profile was established in the pore and, at time = 0, the particle was placed at a centerline position in the pore. Therefore, any resistances at the pore entrance are neglected. Calculations were limited to particles translating along the pore centerline; centerline values for $G(0,\psi)$ were used to describe hydrodynamic resistances at all radial positions in the pore. Finally, torque on the particle was neglected; the translational velocity of the particle was determined using CFD calculations performed with the particle at a fixed orientation; calculations were repeated with the particle at different orientation. To determine $\sigma_f$, the numerically computed $G(0,\psi)$ values were integrated over all sterically allowed particle orientations in Eq. 2. In essence, we have assumed that time scales for rotational diffusion of the particle are much smaller than times for particle translation in the pore. The impact of these assumptions on results is discussed later in this article.

### Numerical model

The fluid forces acting on the particle cause its displacement, and the particle motion in turn changes the fluid profile in the channel. This interplay between fluid and particle motion in this system is incorporated in our model. Incompressible Newtonian fluid flow in a cylindrical channel was simulated using the steady-state Navier-Stokes and continuity equations

$$\rho_f(\boldsymbol{u}\cdot\nabla\boldsymbol{u})=(\nabla\cdot\boldsymbol{\tau}) \tag{4}$$

$$(\nabla\cdot\boldsymbol{u})=0 \tag{5}$$

$$\boldsymbol{\tau}=-p\boldsymbol{I}+\mu_f\left[\nabla\boldsymbol{u}+(\nabla\boldsymbol{u})^T\right] \tag{6}$$

where $\boldsymbol{u}$ is the fluid velocity, $\rho_f$ and $\mu$ are the fluid density and viscosity, respectively, $p$ is the pressure, $\boldsymbol{I}$ is the identity tensor, and $\tau$ is the stress tensor. Here, $\tau$ is the combination of normal and shear forces, which are numerically integrated over the particle surface to determine the total force on the particle[18,20]

$$\boldsymbol{F}=\int(\boldsymbol{\tau}\cdot\boldsymbol{n})d\Gamma \tag{7}$$

The particle velocity is determined using Newton's momentum equation which relates the hydrodynamic forces obtained from the Navier-Stokes equation to the linear momentum of the particle[20]

$$m_p \frac{dv_p}{dt} = \boldsymbol{F} \tag{8}$$

where $m_p$ is the mass of the particle. As noted earlier, the rotational motion caused by the angular momentum is neglected in this analysis; only linear momentum is considered. Equations 4–8 were solved simultaneously using the ALE algorithm, yielding the particle velocity with the particle at a fixed orientation. Rotational diffusion of the particle is implicitly accounted for by calculating particle velocities at all sterically allowed orientations, yielding $G(0,\psi)$ values that are integrated over particle orientation to determine $\sigma_f$ (Eq. 2).

In the ALE algorithm, the particle is tracked in a Lagrangian frame and fluid flow is tracked in a Eulerian reference frame. Therefore, the Navier-Stokes equation must be defined in ALE form. This transformation introduces the mesh velocity $\omega$ in Eq. 4.[18,20,22] The mesh velocity is computed by coupling the Laplace equation with the ALE—Navier-Stokes equation

$$\rho_f((\boldsymbol{u}-\boldsymbol{\omega})\cdot\nabla\boldsymbol{u}) = -\nabla_p + \mu_f\left[\nabla^2\boldsymbol{u}\right] \tag{9}$$

$$(\nabla \cdot \nabla\boldsymbol{\omega}) = 0 \tag{10}$$

Since ALE involves a moving mesh, Eq. 10 ensures a smooth variation in the computational mesh.[20]

For the numerical simulation of the motion of the capsule shaped particle in a cylindrical pore, a 3-D model was developed with geometry illustrated in Figure S1 in the Supplementary Information. Steady Poiseuille flow was established in the pore. At time = 0, an isolated 3-D capsule (cylinder with hemispherical ends) was placed inside the pore at a centerline position. The pore length was set to 10 times the pore diameter. However, the length of the pore is immaterial as long as it is sufficient so that the particle achieves a steady-state velocity within the pore. Since the particle is assumed to be rigid, its trajectory can be tracked using its center of mass.

### *Nondimensional form of model equations*

To nondimensionalize Eqs. 8 and 9, the centerline velocity ($u_c$) in the cylindrical channel and the diameter of the particle ($d_p$) are considered as the characteristic velocity and length, respectively[22]

$$\bar{\boldsymbol{U}} = \frac{\boldsymbol{u}}{u_c} \qquad \bar{t} = \frac{tu_c}{d_p} \tag{11}$$

The resulting nondimensional forms of the Navier-Stokes ALE and Newton's momentum equations are

$$\mathrm{Re}((\bar{\boldsymbol{U}}-\bar{\boldsymbol{\omega}})\cdot\bar{\nabla}\bar{\boldsymbol{U}}) = -\bar{\nabla}\bar{P} + \left[\bar{\nabla}^2\bar{\boldsymbol{U}}\right] \tag{12}$$

$$\left(\mathrm{Re}\bar{\rho}_p\pi\left(\frac{\varepsilon}{4}+\frac{1}{6}\right)\right)\frac{d\bar{\boldsymbol{V}}_{\boldsymbol{p}}}{d\bar{t}} = \bar{\boldsymbol{F}} \tag{13}$$

where *Re* as the Reynolds number, $\bar{\rho}_p$ is the density ratio $\rho_p/\rho_f$ (with a value of 1.1 in these calculations), $\bar{\boldsymbol{V}}_{\boldsymbol{p}}$ is the dimensionless particle velocity, and $\bar{\boldsymbol{F}}$ is the nondimensional hydrodynamic force acting on the particle

$$\mathrm{Re} = \frac{\rho f u_c d_p}{\mu_f} \qquad \bar{P} = \left(\frac{pd_p}{u_c\mu_f}\right) \qquad \bar{\boldsymbol{F}} = \frac{F}{\mu_f u_c d_p} \qquad \bar{\boldsymbol{V}}_{\boldsymbol{p}} = \frac{v_p}{u_c}$$
$$\bar{\nabla} = d_p\nabla \qquad \bar{\nabla}^2 = d_p 2\nabla^2 \tag{14}$$

Equations 12 and 13 were solved, subject to the following boundary conditions. A parabolic velocity field was imposed at z = 0, atmospheric pressure was imposed at the pore exit, and a no slip boundary condition was imposed on the pore wall and on the particle surface. The particle was initially placed on the pore centerline with zero velocity. The particle accelerates due to the fluid forces acting on the particle surface, eventually reaching a steady state velocity when the net forces on the particle are zero.

### *Numerical solution*

The Navier-Stokes ALE equation was coupled with Newton's momentum equation and solved in the computational domain shown in Figure S1. The domain was meshed using tetrahedral elements in the cylindrical volume space and triangular elements on the pore and particle surfaces. To ensure an accurate force calculation, a finer mesh was considered on the particle surface and a coarser mesh in the region away from the particle.

The Navier-Stokes ALE and Newton's momentum equations (Eqs. 12 and 13) were solved using a finite element ALE method.[18–22] The Reynolds number (defined with the particle diameter as the characteristic length scale) was equal to 0.25, consistent with our previous[23] as well as current experiments. Calculations performed with smaller *Re* ($10^{-3}$ to 0.1) showed only a small impact on the lag coefficient (<2% difference), indicating that inertial effects are not important for this system. The translational motion of capsule-shaped particles with different aspect ratios and sizes were considered. In all cases, the particle was positioned at the cylindrical pore axis (centerline approximation) with a fixed orientation. Since torque on the particle was neglected, the particle displays only translational motion in the direction of the fluid flow.

The ALE method involves moving surfaces boundary conditions, which cause the computational mesh to deform. Hence, the Laplace equation was included to ensure a smooth deformation of the mesh. For each time step, the mesh and the particle location were updated, and the mesh quality was checked. Once the quality deteriorated to a set level, a new geometry was generated from the deformed mesh, with the solution from the previous mesh mapped onto the new mesh. The simulation was terminated once the particle attained a steady state velocity and was repeated with the particle positioned at the same initial axial position but with different orientation. The fluid velocity in the absence of the particle $\boldsymbol{u_s}$, was obtained by simulating fluid flow through a 3-D cylindrical channel.

The ALE finite element algorithm was implemented using Comsol Multiphysics 4.2. Comsol's graphical user interface environment cannot directly simulate the moving boundary conditions in this problem. Therefore, the model generated using Comsol was imported to MATLAB to implement an iterative program for auto mesh generation and solution mapping.

The lag coefficient $G(0,\psi)$ was obtained using Eq. 3 with the calculated $\boldsymbol{v_p}$ and $\boldsymbol{u_s}$ values. The rejection coefficient was

**Table 1. Number Weighted Average Size and Degree of Polydispersity of Spherical (Bio)colloids as Determined from Light Scattering Measurements The degree of polydispersity is the normalized variance of the particle diffusion coefficients, as defined by Brown et al.[25]**

| Colloid | Number weighted average size (nm) | Degree of polydispersity |
|---|---|---|
| ST-OL Silica | 48.91 ± 1.67 | 0.067 |
| MP 1040 Silica | 101.1 ± 0.42 | 0.024 |
| MP 2040 Silica | 193 ± 8.76 | 0.026 |
| MP 3040 Silica | 316.44 ± 2.45 | 0.005 |
| PRD1 virus | 80.72 ± 4.94 | 0.157 |
| MS2 virus | 24.75 ± 2.46 | 0.194 |

determined by numerical integration of Eq. 2 using these lag coefficient values. The numerical integrations over pore space and particle orientation were programmed in MATLAB using a Simpson's quadrature technique.

The 3-D model developed using the ALE algorithm was verified using a benchmark problem. The lag coefficient calculated for a sphere translating on the pore axis in a cylindrical pore was reproduced using an appropriate 3-D geometry to represent the system. The steady-state particle velocity and maximum fluid velocity data were extracted from the simulation results to evaluate the lag coefficient; results were compared to an analytical solution available in the literature.[13,24]

## Experimental Methods

### *Spherical colloids*

The number-weighted hydrodynamic diameters of colloidal silica (SNOWTEX-OL Nissan Chemical Industries, Ltd.) and two bacterial viruses (MS2 and PRD1) measured using dynamic light scattering (DLS, BI200SM, Brookhaven Instruments) are given in Table 1. Particle polydispersity is characterized using the degree of polydispersity, which is the normalized variance of the particle diffusion coefficients, as defined by Brown et al.[25] In all cases, the degree of polydispersity was very low, demonstrating the narrow size distribution of these particles.

Silica concentration was measured using light extinction at 600 nm using a 5 cm path length cell (DR 6000, Hach Co.). The bacteriophages MS2 (ATCC 15597-B1) and PRD1 (provided by David Metge at the United States Geological Survey, Boulder, CO) were propagated with the double-top agar layer technique using their respective hosts *Escherichia coli* (ATCC 15597) and *Salmonella typhimurium* (ATCC 19585) as reported earlier by us.[26] Virus stocks were further purified with two successive poly(ethylene glycol) precipitations and chloroform extraction to increase monodispersity and reduce dissolved organic carbon carry over. For filtration experiments, 1 mL of purified virus stock $O$ ($10^{10}$ – $10^{11}$) plaque forming units (PFU)/mL was added to 1 L of feed water to obtain a feed concentration of $O$ ($10^7-10^8$) PFU/mL.

## Bacteria

Cultures of *Escherichia coli, Serratia marcescens,* and *Brevundimonas diminuta* were first grown in Tryptic Soy Broth (TSB; Difco) at 37, 26 and 30°C, respectively and then pelletized by centrifugation at 4°C and 5000 g for 30 min. Bacteria were grown until early stationary phase after resuspending them in phosphate buffered saline (PBS; composition 137 mM NaCl, 2.7 mM KCl, 4.3 mM $Na_2HPO_4.7H_2O$, and 1.4 mM $KH_2PO_4$; pH 7.5), and immediately filtered. Feed concentrations for membrane rejection experiments were maintained in the range $O$ ($10^6-10^7$) colony forming units (CFU)/mL. Bacteria were enumerated by serially diluting the samples, spreading on presolidified trypticase soy agar petri dishes (TSA 1.5%, Difco), and counting 20–300 colonies after 24 h incubation.

The length and diameter of bacteria were obtained by imaging them after fixing with 2.5% glutaraldehyde solution at 4° C overnight. At least 100 cells were inspected. Before electron microscopy (LEO 1525, Carl Zeiss), samples were gently washed with ultrapure water, dehydrated using progressively increasing concentrations of ethanol, and sputter-coated with a 10 nm layer of gold. Bacteria dimensions are listed in Table 2.

### *Membranes*

Pore sizes of polycarbonate hydrophilic track-etched membranes (Isopore, Millipore) were independently measured by image analysis and water permeability. Electron micrographs of membranes were digitally reversed using Image J software so that the background appeared as black and pores were white. The Farsight ToolKit was then used to measure the pore area in square pixels (at least 200 pores from different scale images were analyzed). The pore diameter was calculated by obtaining the pixel size from the scale bar and assuming a circular cross section. Hydraulic equivalent pore diameters were calculated from measurements of pure water fluxes over the pressure range 2–15 psig assuming Poiseuille flow through individual pores and using average pore densities obtained from image analysis. A comparison of pore sizes determined from image analysis, hydraulic permeability and the manufacturer's nominal values is listed in Table 3. Pore sizes determined using image analysis were used when comparing experimental and predicted membrane rejection.

### *Filtration procedure*

Suspensions were dead-end filtered at constant pressure in a cell with 4.1 cm$^2$ effective area (model 8010, Millipore) and very low hold up volume. The pressure (PX303-050G5V, Omega) and cumulative permeate volume (Ohaus Navigator, NIH110, Fisher Scientific) were digitally monitored using LabView (National Instruments, v. 8.5). To reduce concentration polarization and fouling, the filtration cell was continuously stirred at ~ 3000 rpm using a magnetic Teflon bar. First, 100 mL of PBS was passed through the membrane to rinse it before filtering the colloids. Short-term experiments were performed before any fouling could be discerned and rejection was measured after filtering 5 mL

**Table 2. Bacteria Dimensions Measured by Digital Image Analysis**

| Organism | Diameter ($\mu$m) | Length ($\mu$m) | Aspect ratio | Volume equivalent sphere diameter ($\mu$m) |
|---|---|---|---|---|
| *Serratia marcescens* | 0.76 | 1.67 | 2.22 ± 0.58 | 1.07 |
| *Brevundimonas diminuta* | 0.51 | 1.76 | 3.51 ± 0.93 | 0.86 |
| *Escherichia coli* | 0.50 | 2.43 | 4.93 ± 1.2 | 0.95 |

**Table 3. Comparison of Membrane Pore Sizes Determined from Image Analysis and Hydraulic Permeability. Pore sizes determined by SEM imaging were used for comparing measured and predicted particle rejection**

| Nominal pore size (nm) | Image analysis (nm) | Hydraulic permeability (nm) |
|---|---|---|
| 50 | 56.0 ± 8.1 | 72.0 ± 0.5 |
| 100 | 105.5 ± 8.1 | 137.4 ± 1.1 |
| 200 | 166.7 ± 5.0 | 261.1 ± 0.9 |
| 600 | 642.8 ± 20.9 | 747.5 ± 3.7 |
| 800 | 779.5 ± 11.04 | 929.6 ± 15.1 |
| 1200 | 1382.9 ± 105.4 | 1587.7 ± 4.3 |
| 2000 | 1746 ± 92 | 1809.5 ± 4.0 |
| 3000 | 2841.3 ± 135.8 | 2212.7 ± 2.1 |
| 5000 | 3821±421 | 2739.5 ± 13.2 |

of feed water. Biocolloid stocks were diluted in PBS to reduce their $\zeta$ potential to near neutral values (measured to be between $-5$ and $+3$ mV using electrophoretic light scattering, Nicomp 380 ZLS, Particle Sizing Systems), ensuring negligible electrostatic interactions during their passage across membranes.

## Results and Discussion

### *Hydrodynamic interactions using spherical particle model*

As a first approximation, the integrations over pore space and particle orientation in Eq. 2 were carried out by combining previously reported results for the hydrodynamic particle-wall interactions for a spherical particle[17] with the steric restrictions for capsules. Calculations were performed using three different characteristic particle sizes for $G(\alpha, \beta)$: the diameter of a sphere equal to the capsule diameter, the diameter of a sphere equal to the capsule length, and the diameter of a sphere with volume equal to the capsule volume. The dependence of $G(\alpha,\beta)$ on radial position in the pore was included in these calculations.

The ratio of $\sigma_f$ predicted using these approximations to $\sigma_f$ predicted by assuming $G = 1$ is presented in Figure 2 for capsules with aspect ratio = 2 (Figure 2a) and 4 (Figure 2b). As expected, the rejection coefficients calculated with hydrodynamic drag are larger than $\sigma_f$ values predicted with $G = 1$, with the largest rejection coefficients predicted when the capsule length is used as the characteristic particle size for estimating $G$. The ratio of $\sigma_f$ with lag to $\sigma_f$ without lag decreases as particle size increases, with the ratio ~1 for particles with $\lambda > 0.5$ when $\varepsilon = 2$ and $\lambda > 0.3$ when $\varepsilon = 4$. For larger particles, steric restrictions that limit particle positions and orientations within the pore dominate over hydrodynamic resistances experienced by the particle. Hydrodynamic interactions are particularly important for smaller particles ($\lambda < 0.05$), with $\sigma_f$ predicted when incorporating hydrodynamics to be 2–5 times larger than the predictions made by considering only steric interactions.

A comparison of the results presented in Figures 2a and 2b show that predictions of $\sigma_f$ for larger aspect ratio particles are more sensitive to the choice of characteristic particle size used to estimate $G$. Also, adding hydrodynamic resistances has a larger impact on predictions of $\sigma_f$ for the smaller aspect ratio particles. For larger aspect ratio particles, the sterically allowed positions and orientations are significantly reduced when the particle is in a pore, minimizing the effect of hydrodynamic particle pore-wall resistances on $\sigma_f$.

### *CFD simulations: Particle trajectory and velocity*

The CFD calculations yielded the particle displacement in the cylindrical pore domain, from which the particle velocity was calculated. The fluid forces accelerate the initially stationary particle to a steady state velocity. The particle displacement and velocity profile in the pore are illustrated in Figure S2 in the Supplementary Information.

The time evolution of the translational particle velocity for particles oriented with major axis parallel to the pore axis ($\psi = 0$) with $\varepsilon = 2$ and relative particle radii ($\lambda$) of 0.2, 0.5, and 0.8 is shown in Figure 3. Here, $\lambda$ is defined as the ratio of particle diameter to pore diameter. The particle with $\lambda = 0.2$ takes ~0.7 nondimensional time units (equivalent to 2.0 dimensionless length units) to reach a steady-state velocity, whereas the particle with $\lambda = 0.8$ takes 0.05 time units (0.5 dimensionless length units) to achieve steady state. For all cases, the steady-state particle velocity is less than the maximum fluid velocity ($\bar{U}_m$) in the channel in the absence of the particle, due to particle-pore wall interactions.[13,17,27] The steady-state particle velocity is largest for the smallest particles, because the smaller particles are less influenced by

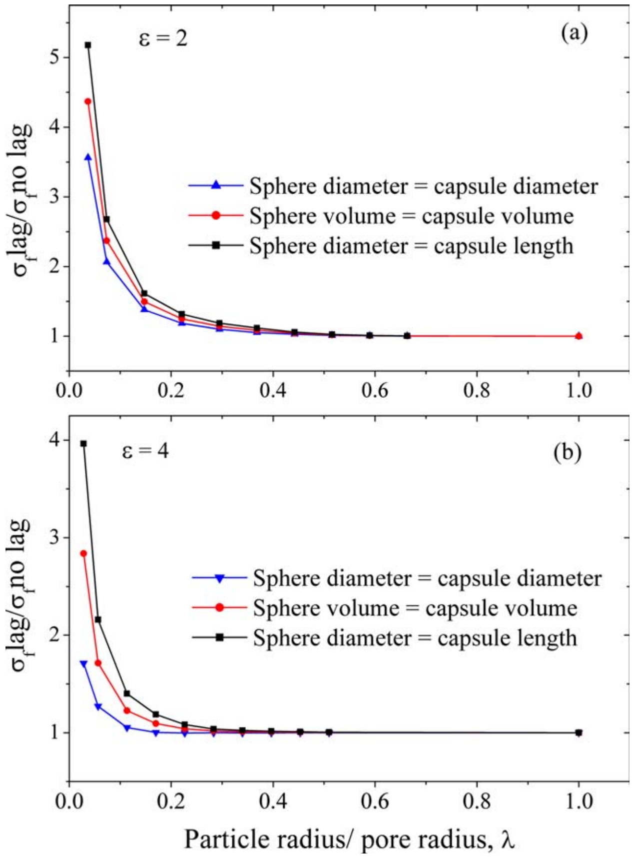

**Figure 2. Effect of incorporating hydrodynamic interactions on predictions of $\sigma_f$ for capsule-shaped particles with (a) aspect ratio = 2, and (b) aspect ratio = 4.**

**(b) Predictions were developed using lag coefficients for a spherical particle with steric restrictions for a capsule. [Color figure can be viewed in the online issue, which is available at wileyonlinelibrary.com.]**

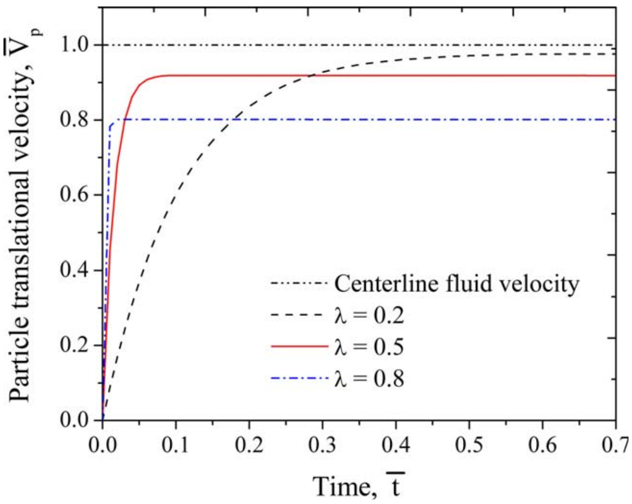

**Figure 3. Time evolution of the translational velocity of a capsule shaped particle in a cylindrical pore when the particle is positioned on the pore axis with orientation angle = 0.**

**Results are shown for a particle with aspect ratio = 2 with $\lambda = 0.2$, 0.5 and 0.8. Here, $\lambda$ is defined as the ratio of particle radius to pore radius. The particle translational velocity is compared with the maximum centerline fluid velocity in the channel $(\bar{U})$. [Color figure can be viewed in the online issue, which is available at wileyonlinelibrary.com.]**

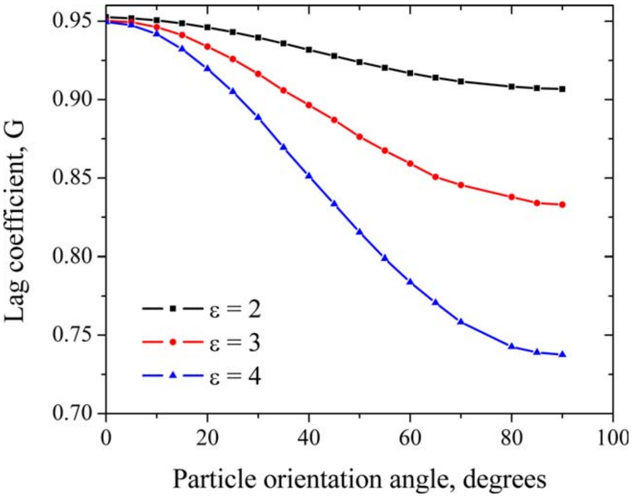

**Figure 4. Effect of particle orientation on the lag coefficient for particles with different aspect ratio ($\varepsilon = 2$, 3 and 4) with $\lambda = 0.2$.**

**[Color figure can be viewed in the online issue, which is available at wileyonlinelibrary.com.]**

the presence of the conduit wall than the larger particles. Particles achieved the same steady state velocity when a nonzero initial velocity was used in the simulation.

### *Effect of particle orientation on the lag coefficient*

Calculations were repeated for particles placed at different orientation angles in the pore, yielding the steady-state particle velocity at each orientation. The lag coefficient $G(0,\psi)$ was determined from the particle and fluid velocities using Eq. 3. The variation of $G(0,\psi)$ with $\psi$ for capsules with $\lambda = 0.2$ and aspect ratios of 2, 3, and 4 is shown in Figure 4. For these particles, all particle orientations from 0° to 90° are sterically allowed. The lag coefficient monotonically decreases with $\psi$ for all $\varepsilon$ values, indicating that the particle experiences the highest hydrodynamic resistance when it is perpendicular to the direction of fluid flow ($\psi = 90°$) and experiences the least resistance at $\psi = 0°$. The difference between $G(0,\psi)$ for $\varepsilon = 2$ and $\varepsilon = 4$ is insignificant at $\psi = 0$, but becomes more pronounced when $\psi$ approaches 90°. Quantitatively, the lag coefficient decreases by 4% for $\varepsilon = 2$ and $\sim$22% for $\varepsilon = 4$, when $\psi$ changes from 0° to 90°. Note that for larger particles, steric restrictions limit the maximum orientation to an angle less than 90°. These limitations are incorporated in the calculations.

### *Effect of lag coefficient on rejection coefficient*

Predictions of $\sigma_f$ from CFD calculations are compared to the no lag model ($G = 1$) in Figure 5 for particles with $\varepsilon = 1$, 2 and 4. A centerline approximation was used to estimate $G$ in the CFD calculations. Here, $\lambda$ is defined using the volume equivalent particle radius, so that all particles with a given $\lambda$ have the same volume. The results show that higher rejections are observed for more elongated particles and that the impact of adding hydrodynamics to the predictions is greatest for spherical particles. As $\lambda$ increases, the difference between predictions made with and without hydrodynamic lag decreases. The steric restrictions that limit the allowed positions and particle orientations dominate over the hydrodynamic particle-pore wall interactions for more elongated and larger particles. These conclusions are qualitatively consistent with the conclusions drawn from the results presented in Figure 2 using the spherical model to approximate hydrodynamic lag.

There are several important assumptions made in our analysis. The first is a centerline approximation, i.e., the lag coefficient at any radial position in the pore is assumed to be equal

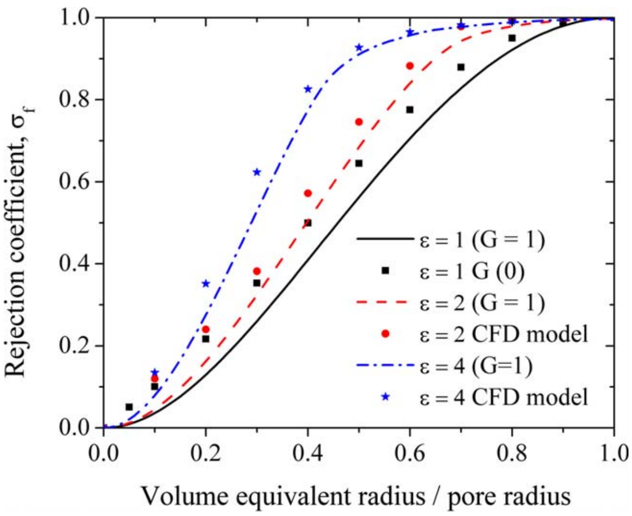

**Figure 5. Impact of hydrodynamic interactions on the rejection coefficient for capsule shaped particles with aspect ratios of 1 (sphere), 2 and 4.**

**CFD calculations were used to determine *G* at different particle orientations for particles along the pore centerline. The rejection coefficient was determined by integrating *G* over the pore space, assuming centerline *G* for all radial positions in the pore. [Color figure can be viewed in the online issue, which is available at wileyonlinelibrary.com.]**

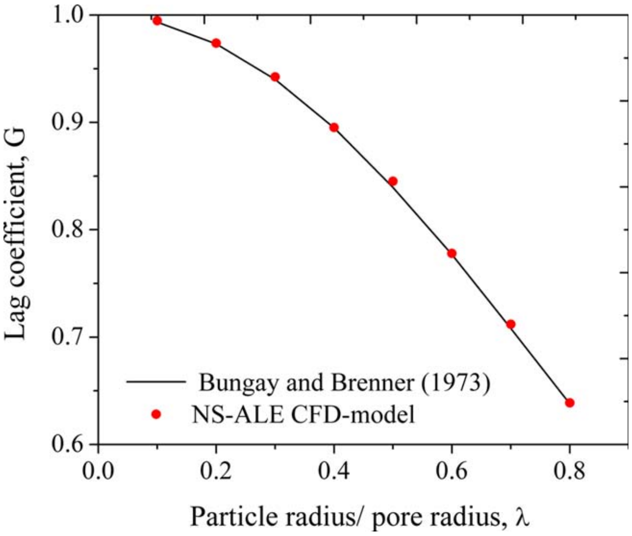

**Figure 6. Validation of the NS—ALE algorithm for the system of a spherical shaped particle translating on the axis of a cylindrical pore using a 3-D model.**

**The solid line is the analytical solution from Bungay and Brenner.[13] [Color figure can be viewed in the online issue, which is available at wileyonlinelibrary.com.]**

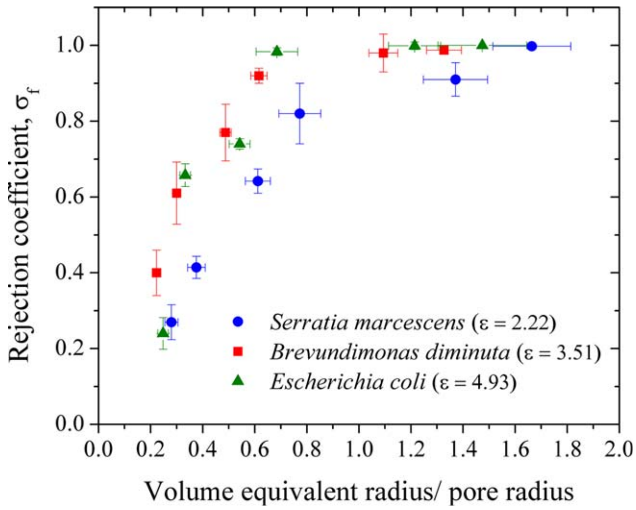

**Figure 8. Experimental membrane rejection results for *S. marcescens* (ε = 2.22), *B. diminuta* (ε = 3.51) and *E. coli* (ε = 4.93).**

**The dimensionless particle size *λ*, is defined using the volume equivalent particle radius. Therefore, data at a fixed *λ* refer to particles with the same volume. [Color figure can be viewed in the online issue, which is available at wileyonlinelibrary.com.]**

to the value on the pore axis. The lag coefficient is largest for a particle at the pore center and decreases as particles move closer to the pore wall. Therefore, this assumptions leads to a lower bound on the predicted reflection coefficient.

The second assumption is that rotational particle diffusion occurs on a much shorter time scale than particle translation, i.e., hydrodynamic torque is neglected. The lag coefficient was determined by calculating the translational particle velocity for capsules at a fixed orientation in the pore. The reflection coefficient was determined by integrating the lag coefficients over all sterically allowed particle orientations. Implicit in this approach is the assumption that all sterically allowed orientation angles are equally probable, i.e., there is no particle alignment in the pores. Particle alignment would yield higher particle velocities and, therefore, larger lag coefficients and smaller rejection coefficients. This assumption leads to an upper bound on the rejection coefficient.

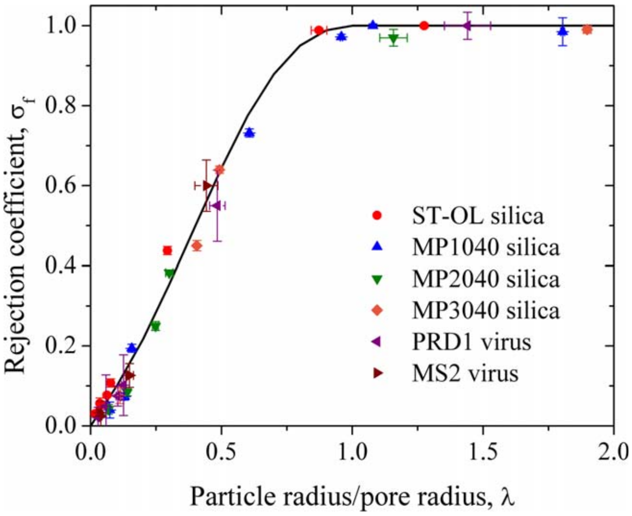

**Figure 7. Comparison of experimental results for spherical particles with theoretical predictions of the rejection coefficient.**

**Model predictions were made using a centerline approximation for the lag coefficient of a sphere.[13] [Color figure can be viewed in the online issue, which is available at wileyonlinelibrary.com.]**

Another assumption made in our analysis is that the particle concentration is dictated by a Boltzmann probability and any pore entrance effects that might alter the concentration profile are neglected. The impact of pore entrance effects was examined by Quddus et al.[18] for spherical particles who found the ratio of *G* at the pore entrance to *G* at a distance inside the pore to be ~0.95 for particles of various sizes located along the pore axis. These results indicate that a particle experiences minimal resistance when entering the pore. However, for a nonspherical particle, entrance effects may lead to particle alignment which is not accounted for in our model. We plan to use CFD simulations to examine the transport of capsule shaped particles from a reservoir into a pore to better understand the impact of pore entrance effects on particle transport in a pore.

### *CFD code validation*

To validate the Navier-Stokes ALE code, lag coefficients for a sphere translating along the axis of a cylindrical pore were calculated. For the same system, Bungay and Brenner developed an analytical solution using a perturbation technique and asymptotic expansion.[13] A comparison of *G* determined from the CFD calculations to Bungay and Brenner's solution shows excellent agreement between the CFD results and the analytical solution, validating the Navier-Stokes ALE algorithm developed in this work. CFD results and the analytical solution are compared in Figure 6.

### *Experimental results*

*Spherical Particles.* A comparison of the experimentally measured membrane rejection coefficients for spherical silica colloids and the spherical virus particles PRD1 and MS2 to model predictions is shown in Figure 7. The model predictions were generated using the centerline approximation ($G(X) = G(0)$). Excellent agreement was observed between data and experiment for both virus and silica particles for the entire range of dimensionless particle sizes, confirming the validity of the pore size values and the experimental procedures used for the rejection measurements.

*Bacteria.* Experimental membrane rejection data for *S. marcescens* ($\varepsilon = 2.22$), *B. diminuta* ($\varepsilon = 3.51$) and *E. coli* ($\varepsilon = 4.93$) are compared in Figure 8. Experimental results were generated using membranes with different pore sizes, yielding results over a range of dimensionless particle sizes. The results generally follow the trends predicted from our model, with increasing rejection as aspect ratio increases at a fixed value of $\lambda$.

In our earlier publication,[23] experimental results for four different nonspherical bacteria and viruses with aspect ratio ranging from 2.7 to 8.9 showed measured rejection coefficients that were generally independent of particle aspect ratio, results that are not consistent with those presented in Figure 8. In the previous work, the aspect ratio for three of the particles ranged from 2.7 to 4.0, differences that, according to our model, are not expected to yield significant differences in rejection. The fourth particle was a unique *B. diminuta* that, because of growth conditions had an aspect ratio of 8.9. This elongated particle may have become aligned with the flow in the pores, yielding lower rejections than predicted from both the steric restrictions model ($G = 1$) as well as the current CFD model that includes hydrodynamic resistances.

Comparisons of the experimentally measured membrane rejection coefficients to model predictions are shown in Figure 9 with comparisons for *S. marcescens* in Figure 9a, for *B. diminuta* in Figure 9b and for *E. coli* in Figure 9c. The theoretical predictions were obtained from our CFD calculations using the appropriate aspect ratio for each particle.

The comparisons in Figure 9 show generally good agreement between experiment and theory for all systems. The increase in rejection observed as $\lambda$ increases (i.e., decreasing pore size) follows the rate of increase predicted by the model. Complete rejection is observed for experiments with small pore membranes ($\lambda > 1$). Note that the volume equivalent sphere radius is used here to define $\lambda$. Therefore, with appropriate orientation, the particles could access the pore even when $\lambda > 1$, but do not to any significant extent, as predicted by the model.

The comparisons in Figure 9 also show that in all cases, measured rejection values were less than or equal to model predictions. There were no experimental rejection coefficients larger than predicted values. Particle alignment in the pores, which was neglected in the CFD calculations, may be responsible for this trend. Our current efforts are focused on a model that includes torque on the particles. Results from this revised model may help us to better understand these observations.

Long-range particle—pore-wall interactions were also neglected in the CFD model. Attractive particle—pore-wall interactions could result in higher-particle concentrations in the pore, yielding reduced membrane rejections relative to values predicted when only steric interactions are considered. Experimentally, buffer conditions were established to keep particle $\zeta$ potential at near neutral conditions. Future experiments will examine rejection with different ionic strength buffers. Results from these measurements may also help us to better understand our observations. A revised model that includes particle—pore-wall electrostatic interactions will also be developed.

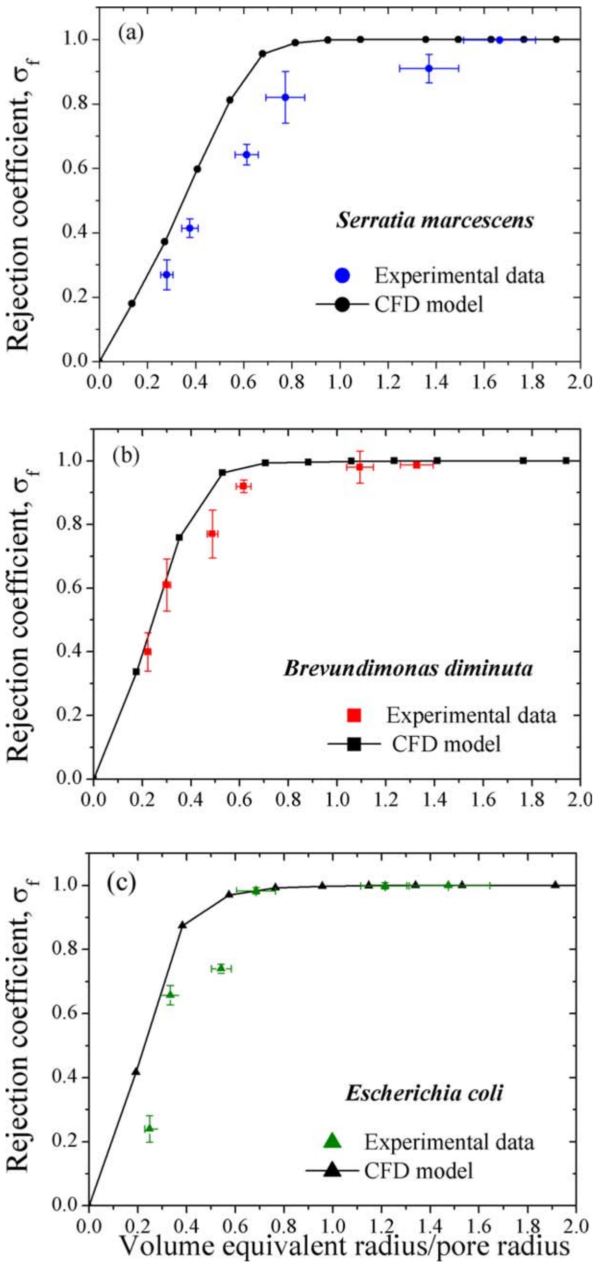

**Figure 9. Comparison of experimental results with theoretical predictions of the rejection coefficient for (a) *S. marcescens* ($\varepsilon = 2.22$, compared to a model with $\varepsilon = 2.0$), (b) *B. diminuta* ($\varepsilon = 3.5$, compared to a model with $\varepsilon = 3.5$), and (c) *E. coli* ($\varepsilon = 4.93$, compared to a model with $\varepsilon = 5.0$).**

**Model predictions were made using CFD calculations for the lag coefficient *G*. [Color figure can be viewed in the online issue, which is available at wileyonlinelibrary.com.]**

## Summary and Conclusions

The effect of convective hydrodynamic resistances on the reflection coefficient for a capsule shaped particle in a cylindrical pore has been examined using an approximate model based on the hydrodynamic resistances experienced by a sphere and from CFD calculations for a capsule. Predictions of $\sigma_f$ from the CFD model are in close agreement with the sphere model when the hydrodynamic hindrance for a rod is approximated using a sphere whose diameter equals the capsule length. However, it should be noted that the lag coefficient calculated using the CFD model is based on a centerline approximation, whereas the sphere model includes the radial dependence of the lag coefficient.

Results reveal that the addition of convective hindrance to steric considerations within the pore increases predicted $\sigma_f$ values for small particles, but has minimal impact for larger particles. Incorporating hydrodynamic resistances also has a larger impact for particles with a smaller aspect ratio (closer to a sphere). Steric considerations apparently dominate for large and more elongated particles.

Experimental results collected from filtration experiments performed with track etch polycarbonate membranes and three different bacteria with aspect ratio ranging from 2.2 to 5 show generally good agreement between model predictions and experimentally observed membrane rejection coefficients.

The CFD calculations presented here were limited to particles positioned at the pore centerline. To accurately evaluate the lag coefficient for a capsule shaped particle at off-axis positions, torque-induced rotation should be considered because of the high-shear rates near the pore wall. We are currently developing such a model. A revised model that incorporates long-range electrostatic particle—pore-wall interactions is also being developed.

From a practical perspective, the current results indicate that selection of a pore size needed to achieve a desired level of rejection of capsule-shaped microorganisms is not particularly sensitive to whether or not hydrodynamic interactions are included in the model predictions, particularly for high rejection systems (>0.5). Selection of pore size using a no lag model or a model based on a spherical approximation for the hydrodynamic lag coefficient provides a conservative estimate that should not have a significant impact on energy requirements for a given system.

## Notation

| | |
|---|---|
| $d_p$ | diameter of capsule shaped particle, $\mu$m |
| $E$ | interaction energy between particle pore wall, J/mol |
| $\mathbf{F}$ | fluid force on the particle surface, N |
| $\bar{\mathbf{F}}$ | dimensionless fluid force on the particle surface |
| $G$ | lag coefficient |
| $L$ | cylinder length, $\mu$m |
| $L_p$ | length of a capsule shaped particle, $\mu$m |
| $m_p$ | particle mass, g |
| $p$ | pressure, N/m$^2$ |
| $\bar{P}$ | dimensionless pressure |
| $R$ | pore radius, $\mu$m |
| $Re$ | Reynolds number |
| $t$ | time, s |
| $\bar{t}$ | dimensionless time |
| $\mathbf{u}$ | fluid velocity, m/s |
| $\mathbf{u_s}$ | streamline fluid velocity, m/s |
| $u_c$ | centerline fluid velocity, m/s |
| $\bar{\mathbf{U}}$ | dimensionless fluid velocity |
| $v(X)$ | velocity field, m$^2$ |
| $v_p$ | particle velocity, m/s |
| $\bar{\mathbf{V}}_\mathbf{p}$ | dimensionless particle velocity |
| $X(x,y)$ | 2-D position vector |
| $\sigma_f$ | filtration rejection coefficient |
| $\psi$ | particle orientation angle, degrees |
| $\alpha,\beta$ | dimensionless Cartesian coordinates |
| $\lambda$ | dimensionless particle size |
| $\varepsilon$ | particle aspect ratio ($L_p/d_p$) |
| $\rho_f$ | fluid density, kg/m$^3$ |
| $\rho_p$ | particle density, kg/m$^3$ |
| $\bar{\rho}_p$ | dimensionless particle density |
| $\tau$ | stress tensor, N/m$^2$ |
| $\mu_f$ | fluid viscosity N s/m$^2$ |
| $\omega$ | mesh velocity, m/s |
| $\bar{\boldsymbol{\omega}}$ | dimensionless mesh velocity |
| $\nabla$ | Laplace operator |

## Acknowledgment

The authors gratefully acknowledge the support from the National Science Foundation through grants CBET-0966934 and CBET-0966939.

## Literature Cited

1. Zeman LJ, Zydney AL. *Microfiltraction and Ultrafiltraction: Principles and Application*. New York: Dekker; 1996.
2. Kramer MH, Herwaldt BL, Craun GF, Calderon RL, Juranek DD. Waterborne disease: 1993 and 1994. *AWWA*. 1996;88(3):66–80.
3. Jacangelo JG, Adham SS, Laine JM. Mechanisim of cryptosporidum, Giarida and MS2 Viral Removal By MF and UF. *AWWA*. 1995;87(9):107–121.
4. Mi B, Mariñas BJ, Curl J, Sethi S, Crozes G, Hugaboom D. Microbial passage in low pressure membrane elements with compromised integrity. *Environ Sci Technol*. 2005;39(11):4270–4279.
5. Madaeni SS, Fane AG, Grohmann GS. Virus removal from water and wastewater using membranes. *J Membr Sci*. 1995;102(0):65–75.
6. Urase T, Yamamoto K, Ohgaki S. Effect of pore structure of membranes and module configuration on virus retention. *J Membr Sci*. 1996;115(1):21–29.
7. Sadr Ghayeni SB, Beatson PJ, Fane AJ, Schneider RP. Bacterial passage through microfiltration membranes in wastewater applications. *J Membr Sci*. 1999;153(1):71–82.
8. Jornitz MW, Meltzer TH. *Sterile Filtration: A Practical Approach:* Informa Healthcare; 2001.
9. Anderson JL, Quinn JA. Restricted transport in small pores: A model for steric exclusion and hindered particle motion. *Biophys J*. 1974;14:130–150.
10. Deen WM. Hindrance transport of large molecules in liquid filled pores. *AIChE J*. 1987;33:1409–1425.
11. Anderson JL. Configurational effect on the reflection coefficient for rigid solutes in capillary pore. *J Theor Biol*. 1981;90:405–426.
12. Anderson JL, Malone DM. Mechanism of osmotic flow in porous membranes. *Biophys J*. 1974;14(12):957–982.
13. Bungay PM, Brenner H. The motion of a closely-fitting sphere in a fluid-filled tube. *Int J Multiphase Flow*. 1973;1(1):25–56.
14. Brenner H, Gaydos LJ. The constrained Brownian movement of spherical particles in cylindrical pores of comparable radius: Models of the diffusive and convective transport of solute molecules in membranes and porous media. *J Colloid Interface Sci*. 1977;58(2): 312–356.
15. Ennis J, Zhang H, Stevens G, Perera J, Scales P, Carnie S. Mobility of protein through a porous membrane. *J Membr Sci*. 1996;119(1): 47–58.
16. Higdon JJL, Muldowney GP. Resistance functions for spherical particles, droplets and bubbles in cylindrical tubes. *J Fluid Mech*. 1995;298:193–210.
17. Dechadilok P, Deen WM. Hindrance factors for diffusion and convection in pores. *Ind Eng Chem Res*. 2006;45(21):6953–6959.
18. Al Quddus N, Moussa WA, Bhattacharjee S. Motion of a spherical particle in a cylindrical channel using arbitrary Lagrangian-Eulerian method. *J Colloid Interface Sci*. 2008;317(2):620–630.
19. Nomura T, Hughes, T.J. An arbitrary Lagrangian-Eulerian finite element method for interaction of fluid and a rigid body. *Comput Methods Appl Mech Eng*. 1992;95:115–138.
20. Ai Y, Joo SW, Jiang Y, Xuan X, Qian S. Pressure-driven transport of particles through a converging-diverging microchannel. *Biomicrofluidics*. 2009;3(2):022404–022414.

21. Donea J HA, Ponthot J P, Rodriguez A, Stien.E, Borst R de, Huges JR, eds. *Encyclopedia of computational mechanices*. Vol 1. Hoboken, NJ: John Wiley & Sons; 2004:chap14.
22. Dinesh J. Modelling and simulation of a single particle in laminar flow regime of a newtonian liquid. COMSOL Conference. Bangalore, *India;* 2009.
23. Baltus RE, Badireddy AR, W X, Chellam S. Analysis of configurational effects on the hindrance convective non spherical bacteria and viruses across microfiltration membranes. *Ind Eng Chem Res.* 2009;298:193–210.
24. Haberman WL, Sayre RM, David WTMBHL. *Motion of Rigid and Fluid Spheres in Stationary and Moving Liquids Inside Cylindrical Tubes*. Washington DC: Dept of the Navy, David Taylor Model Basin; 1958.
25. Brown J, Pusey PN, Dietz R. Photon correlation study of polydisperse samples of polystyrene in cyclohexane. *J Chem Phys.* 1975;62(3):1136–1144.
26. Tanneru CT, Chellam S. Mechanisms of virus control during iron electrocoagulation - Microfiltration of surface water. *Water Res.* 2012;46(7):2111–2120.
27. Happel J, Brenner H. *Low Reynolds Number Hydrodynamics*: The Netherlands: Noordhoff International Publishing; 1973.

## Appendix

## Derivation of Eq. 2

In this Appendix, the derivation of Eq. 2 from Eq. 1 is presented, following the development presented by Anderson.[11] For laminar flow in a cylindrical pore with pore radius $R$, the velocity field is

$$v(X)=\frac{1}{4}\left(r^2-R^2\right)=\frac{1}{4}\left[x^2+y^2-R^2\right] \tag{A1}$$

The volume of orientation space is

$$d\hat{\boldsymbol{e}}=\sin\psi\ d\psi\ d\varphi \tag{A2}$$

Here $\psi$ is the solid angle between the orientation unit vector $\hat{\boldsymbol{e}}$ and the $z$ axis, and $\varphi$ is the azimuthal angle. Substituting Eqs. A1 and A2 into Eq. 1 and applying steric potential conditions ($E(X,\psi)=0$ when the particle is positioned completely inside the pore $(x,y,\psi,\varphi)$ and $E(X,\psi)=\infty$ if the particle penetrates the pore wall when the particle center is located at $(x,y,\psi,\varphi)$) yields

$$\sigma_f=1-\frac{8}{4\pi R^4}\int_0^{\pi}\int_0^{\frac{\pi}{2}}\int_0^{x_{\max}}\int_0^{y_{\max}} G(x,y,\psi)\,\frac{1}{4}\left[x^2+y^2-R^2\right]\,dx\ dy\ \sin(\psi)d\psi\ d\varphi \tag{A3}$$

where $x_{\max}$ and $y_{\max}$ are the upper limits for the particle position within the pore space, which depend on the particle orientation, $\psi$. For a capsule particle, $x_{\max}$ and $y_{\max}$ are

$$x_{\max}=\sqrt{R'^2-L'^2}\qquad y_{\max}=\sqrt{R'^2-x^2}-L'^2$$

$$L'=\frac{L_p-L_0}{2}\sin(\psi)\qquad R'=R-\frac{L_0}{2}$$

$$L_0=L_p-d_p$$

We define dimensionless coordinates $\alpha$ and $\beta$ by

$$\alpha=\frac{x}{R}\qquad \beta=\frac{y}{R}$$

yielding

$$L^*=(\varepsilon-1)\lambda\sin(\psi)\qquad R^*=(1-\lambda)$$

$$\varepsilon=\frac{L_p}{d_p}\qquad \lambda=\frac{d_p}{2R}$$

$$\alpha_{\max}=\sqrt{R^{*2}-L^{*2}}\qquad \beta_{\max}=\sqrt{R^{*2}-\alpha^2}-L^{*2}$$

Substituting these dimensionless parameters into Eq. A3 yields

$$\sigma_f=1-\frac{8}{\pi}\int_0^{\frac{\pi}{2}}\int_0^{\alpha_{\max}}\int_0^{\beta_{\max}} G(\alpha,\beta,\psi)\left[\alpha^2+\beta^2+1\right]d\beta d\alpha\sin(\psi)d\psi \tag{A4}$$

which is Eq. 2.

*Manuscript received Jul. 5, 2012, and revision received Mar. 3, 2013.*